A Time-Domain Differential Solver for Electromagnetic Scattering Problems

VIJAYA SHANKAR, WILLIAM F. HALL, AND ALIREZA H. MOHAMMADIAN, MEMBER, IEEE

The objective of this paper is to extend computational fluid dynamics (CFD) based upwind schemes to solve numerically the Maxwell equations for scattering from objects with layered nonmetallic sections. After a discussion on the character of the Maxwell equations it is shown that they represent a linearly degenerate set of hyperbolic equations. To show the feasibility for applying CFD-based algorithms, first the transverse magnetic (TM) and the transverse electric (TE) waveforms of the Maxwell equations are considered. A finite-volume scheme is developed with appropriate representations for the electric and magnetic fluxes at a cell interface, accounting for variations in material properties in both space and time. This process involves a characteristic subpath integration known as the "Riemann solver." An explicit Lax-Wendroff upwind scheme, which is second-order accurate in both space and time, is employed to solve the TM and TE equations. A body-fitted coordinate transformation is introduced to treat arbitrary cross-sectioned bodies with computational grids generated using an elliptic grid solver procedure. For treatment of layered media, a multizonal representation is employed satisfying appropriate zonal boundary conditions in terms of flux conservation. The computational solution extending from the object to a far-field boundary located a few wavelengths away constitutes the near-field solution. A Green's function based near-field-to-far-field transformation is employed to obtain the bistatic radar cross section (RCS) information. Results are presented for a number of two-dimensional objects with layered structures for both continuous wave (single-frequency, time harmonic) and transient (broad-band frequency response) cases. The time-domain solver also provides a unique capability for including nonlinear and time-varying material properties.

I. Introduction

The radar return from complex structures has traditionally been calculated by one of two methods: high-frequency asymptotics, which treats scattering and diffraction as local phenomena; or solution of an integral equation for radiating sources on (or inside) the scattering body, which couples all parts of the body through multiple scattering processes. In this paper we describe a third alternative, the direct integration of the differential form of Maxwell's equations in time.

The time-domain Maxwell equations represent a more general form than the frequency-domain Helmholtz equations, which are usually restricted to solving scattering problems having time harmonic fields, whereas a time-domain approach can handle continuous waves (single frequency, harmonic) as well as a single-pulse (broad-band frequency) transient response. Frequency-domain-based methods usually provide the radar cross section (RCS) response for all angles of incidence at a single frequency, while time-domain-based methods provide solutions for many frequencies from a single transient calculation. Also, in a time-domain approach one can consider time-varying material properties for the treatment of active surfaces. Using spectral methods, the time-domain transient solutions can be processed to provide the frequency-domain response.

In the present work, it has been our aim to accurately predict the scattering from bodies that include regions with dielectric and magnetic properties significantly different from those of free space. Configurations involving coated inlets, composite radar-absorbing airfoils, and multiple layers of material are typical of many modern aircraft and missiles, and their scattering properties often range over several orders of magnitude as a function of incident and reflected angles.

There are many ways one can solve the time-domain Maxwell equations numerically [1]-[8]. Most notably, the work of Taflove and Umashankar [3]-[6] employs a finite-difference method developed by Yee [1]. The approach to be followed in this paper is to utilize the numerical algorithms that have been proven most successful in integrating the time-dependent equations of fluid dynamics, namely, the Euler and the Navier-Stokes equations [9]-[18]. Computational algorithms to solve these nonlinear equations of fluid dynamics have progressed rapidly over the last 20 years, and many of these computational fluid dynamics (CFD) methods are directly applicable to computational electromagnetics (CEM) in solving Maxwell's equations. Some of the attributes of CFD methods that can be employed effectively to design a time-domain differential solver for Maxwell's equations are listed here.

1) The fluid dynamic equations are usually cast in a conservation form (to be described later) conserving mass, momentum, and energy fluxes, thus allowing for numerical capture of flow discontinuities such as shocks and slip surfaces. The Maxwell equations also can be cast in a conservation form. In this particular form, they are naturally

Manuscript received May 26, 1988; revised November 4, 1988. This work was supported by Rockwell North American Aviation.

The authors are with the Science Center, Rockwell International Corporation, Thousand Oaks, CA 91360, USA.

IEEE Log Number 8927965.

0018-9219/89/0500-0709$01.00 © 1989 IEEE

structured for numerical simulation of scattering from objects with layered media having discontinuous or gradually varying material properties.

2) Recent developments of hyperbolic algorithms [13]–[18] for solving the time-domain Euler equations are based on the characteristic theory of signal propagation and are referred to as the "upwind" schemes. For hyperbolic equations, the upwind-based schemes can be constructed to provide the right amount of numerical dissipation to achieve both stability and accuracy of computation. The time-domain Maxwell equations, which are hyperbolic in character (to be shown later), can also benefit from employing such upwind type schemes.

3) For the treatment of complex aerospace configuration geometries, CFD methods usually employ a body-fitted coordinate system for easy implementation of boundary conditions. Concepts such as numerical grid generation for a body-fitted system, multizoning [15], adaptive gridding, etc., are well suited for CEM, especially when the scatterer is an aerodynamic object for which the CFD methods are applied. However, the gridding requirements for a desired field resolution may be different for CEM applications (frequency dependent) from that of CFD needs. Also, CEM problems may involve internal/external layered structures, requiring more involved multizone gridding procedures.

4) There are several proven discretizable procedures in use in CFD for solving the nonlinear fluid dynamic equations. Many discretization concepts, such as finite-difference, finite-volume, and finite-element schemes [9]–[17], implicit and explicit time-stepping procedures [19], and relaxation and approximate factorization techniques [9], are equally applicable to solving the Maxwell equations.

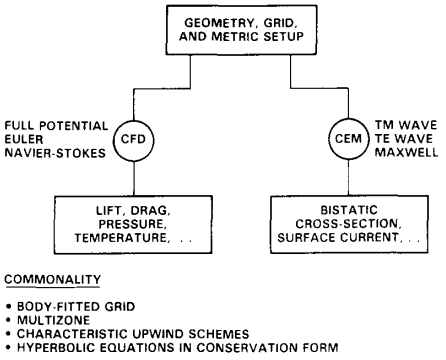

Fig. 1. Commonality between CEM and CFD.

In general, many ideas are in common between CEM and CFD. This is illustrated schematically in Fig. 1. Even the pre- and postprocessing graphics packages developed for CFD solutions satisfy the needs of CEM. Thus, our approach is to utilize the numerical algorithms that have proven most successful in integrating the time-dependent equations of fluid dynamics to solve Maxwell's equations.

II. Equations in Conservation Form

As mentioned in the Introduction, many problems in mathematical physics are governed by an appropriate set of partial differential equations. The Navier–Stokes equations in fluid dynamics and the Maxwell equations in electromagnetics are two specific examples. In general, many equations in mathematical physics naturally lend themselves to a conservation form representation given by

$$Q_t + E_x + F_y + G_z = S \tag{1}$$

where the solution vector Q, the source S, and the flux vectors E, F, and G take on different forms depending on the physical problem being modeled. In Eq. (1), the subscripts t, x, y, and z denote partial derivatives. Implementation of Eq. (1) in many realistic problems requires a coordinate transformation to properly represent the physical domain of interest and to aid in the boundary condition treatment.

Under the transformation of coordinates implied by

$$\tau = t, \quad \xi = \xi(t, x, y, z), \quad \eta = \eta(t, x, y, z),$$
$$\zeta = \zeta(t, x, y, z)$$

Eq. (1) can be recast in the conservation form given by

$$\overline{Q}_\tau + \overline{E}_\xi + \overline{F}_\eta + \overline{G}_\zeta = \overline{S} \tag{2}$$

where $\overline{Q} = Q/J$, $\overline{E} = (Q\xi_t + E\xi_x + F\xi_y + G\xi_z)/J$, $\overline{F} = (Q\eta_t + E\eta_x + F\eta_y + G\eta_z)/J$, $\overline{G} = (Q\zeta_t + E\zeta_x + F\zeta_y + G\zeta_z)/J$, and $\overline{S} = S/J$, with J being the Jacobian of the transformation

$$J = \frac{\partial(\xi, \eta, \zeta)}{\partial(x, y, z)}.$$

Fig. 2 schematically illustrates a body-fitted system in two dimensions.

Associating the subscripts j, k, l with the ξ, η, ζ directions, a numerical approximation to Eq. (2) may be expressed in the semidiscrete conservation law form given by

$$(\hat{Q}_{j,k,l})_\tau + (\hat{E}_{j+1/2,k,l} - \hat{E}_{j-1/2,k,l}) + (\hat{F}_{j,k+1/2,l} - \hat{F}_{j,k-1/2,l}) + (\hat{G}_{j,k,l+1/2} - \hat{G}_{j,k,l-1/2}) = \hat{S}_{j,k,l} \tag{3}$$

where $\hat{E}$, $\hat{F}$, $\hat{G}$ are numerical or representative fluxes at the bounding sides of the cell for which discrete conservation is considered, and $\hat{Q}_{j,k,l}$ is the representative conserved quantity (the numerical approximation to $\overline{Q}$) considered conveniently to be the centroidal value. The half-integer subscripts denote cell sides and the integer subscripts the cell itself or its centroid. Fig. 3 illustrates the nomenclature associated with a finite-volume cell. The concept of upwinding, to be described subsequently, will be employed in the evaluation of fluxes at interfaces.

The objective is to solve Eq. (3) for the dependent vector Q. After the incorporation of proper flux representation, the discrete form of Eq. (3) can be written as

$$R(Q) = 0. \tag{4}$$

If Q is known to lie in the neighborhood of a given state, denoted by Q^*, then the solution to Eq. (4) can be written to first order in $Q - Q^*$ as

$$\frac{\partial R}{\partial Q}(Q - Q^*) = -R(Q^*) \tag{5}$$

where $\partial R/\partial Q$, in general, is a differential operator. Many numerical algorithmic issues, such as implicit methods, explicit methods, relaxation schemes, and approximate factorization procedures, come into play in the modeling of the differential operator $\partial R/\partial Q$. Issues such as higher order

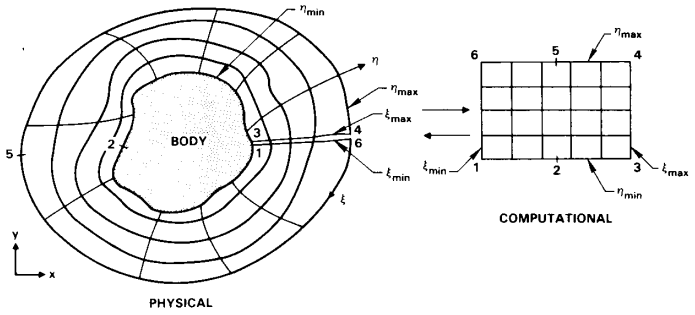

Fig. 2. Schematic of a body-fitted system.

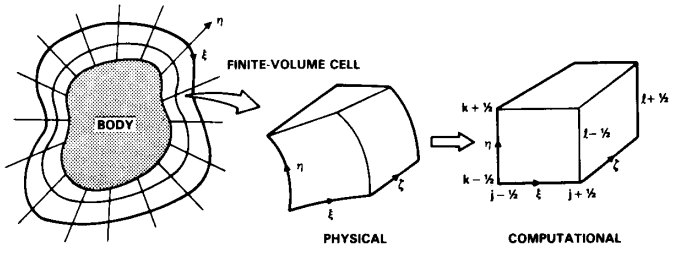

Fig. 3. Nomenclature associated with a finite-volume cell.

accuracy, efficiency, proper upwinding, and treatment of discontinuities come into $\partial R/\partial Q$ as well as in the modeling of the right-hand side $R(Q^*)$.

The objective of this paper is to apply CFD-based finite-volume numerical methods developed for solving many nonlinear gasdynamic equations [9]–[19] to solve the time-dependent Maxwell equations for electromagnetic scattering problems involving layered material media.

III. Maxwell's Equations

Analysis of electromagnetic scattering from permeable (dielectric and lossy media) and impermeable (metallic) objects is of interest in being able to predict the RCS of low observable aerospace configurations. The equations that govern the interaction between electric and magnetic fields are the Maxwell equations. These equations in their vector form are

$$\frac{\partial B}{\partial t} = -\nabla \times \mathcal{E}$$

$$\frac{\partial D}{\partial t} = \nabla \times \mathcal{H} - J. \tag{6}$$

The vector quantities $\mathcal{E} = (\mathcal{E}_x, \mathcal{E}_y, \mathcal{E}_z)$ and $\mathcal{H} = (\mathcal{H}_x, \mathcal{H}_y, \mathcal{H}_z)$ are the electric and magnetic field intensities, $D = (D_x, D_y, D_z)$ is the electric displacement, $B = (B_x, B_y, B_z)$ is the magnetic induction, and $J = (J_x, J_y, J_z)$ is the current density. The subscripts x, y, z in the vector representation of $\mathcal{E}$, $\mathcal{H}$, B, and D refer to components in the respective directions.

In order to apply CFD-based conservation-law form finite-volume methods, Eq. (6) is rewritten in the form of Eq. (1). For isotropic materials, the solution vector Q and the flux vectors E, F, and G are given by

$$Q = \begin{Bmatrix} B_x \\ B_y \\ B_z \\ D_x \\ D_y \\ D_z \end{Bmatrix}, \qquad E = \begin{Bmatrix} 0 \\ -D_z/\epsilon \\ D_y/\epsilon \\ 0 \\ B_z/\mu \\ -B_y/\mu \end{Bmatrix},$$

$$F = \begin{Bmatrix} D_z/\epsilon \\ 0 \\ -D_x/\epsilon \\ -B_z/\mu \\ 0 \\ B_x/\mu \end{Bmatrix}, \qquad G = \begin{Bmatrix} -D_y/\epsilon \\ D_x/\epsilon \\ 0 \\ B_y/\mu \\ -B_x/\mu \\ 0 \end{Bmatrix},$$

$$S = \begin{Bmatrix} 0 \\ 0 \\ 0 \\ -J_x \\ -J_y \\ -J_z \end{Bmatrix}. \tag{7}$$

The permittivity coefficient ϵ and the permeability coefficient μ are the material properties and satisfy the relationships $D = \epsilon\mathcal{E}$ and $B = \mu\mathcal{H}$. The current density J is usually represented by $\sigma\mathcal{E}$, where σ is the material electrical conductivity. The objective is to solve Eq. (7) to predict the electromagnetic scattering from objects with layered structure for a given incident field (continuous wave or a pulse). From the time variation of the scattered field, the RCS of the scatterer can be obtained.

IV. Characteristic Theory for Maxwell's Equations

The application of a finite-volume procedure, Eq. (3), for the Maxwell equations, Eq. (7), requires the evaluation of the various fluxes $\hat{E}$, $\hat{F}$, and $\hat{G}$ at cell interfaces from the solution vector $\hat{Q}$ known at cell centroids. There are many ways one can represent these fluxes, depending on the choice of numerical algorithms, such as central difference schemes and upwind schemes. The choice and construction of a numerical algorithm involve many issues, such as accuracy, efficiency, numerical stability, storage requirements, and treatment of discontinuities in the solution field (shocks in fluid dynamics, discontinuous material properties in electromagnetics). In CFD, upwind-based methods that take into account the theory of characteristic signal propagation are widely in use. Some of the background information on upwind-based schemes is provided in [13]–[18]. The objective of the present work is to adapt the upwind-based algorithms of CFD to solve the Maxwell equations.

First, the character of the Maxwell equations is analyzed to aid in the development of a proper upwind scheme for electromagnetic flux representation. This section provides the characteristic theory framework for the one-dimensional Maxwell equations.

Consider the following conservation form [one-dimensional form of Eq. (7)]:

$$\frac{\partial Q}{\partial t} + \frac{\partial E(Q)}{\partial x} = S \tag{8}$$

where

$$Q = \begin{pmatrix} D \\ B \\ e \\ m \end{pmatrix}, \quad E = \begin{pmatrix} -Bm \\ -De \\ 0 \\ 0 \end{pmatrix}, \quad S = \begin{pmatrix} -J \\ 0 \\ \dot{e}(t) \\ \dot{m}(t) \end{pmatrix}$$

and the material properties ϵ and μ are represented by $e = 1/\epsilon$ and $m = 1/\mu$, respectively.

The character of Eq. (8) is described by the eigenvalues and the eigenvectors of the Jacobian of E given by $A = \partial E/\partial Q$. The eigenvalues of A are first obtained by solving $|A - \lambda I| = 0$,

$$A = \frac{\partial E}{\partial Q} = \begin{vmatrix} 0 & -m & 0 & -B \\ -e & 0 & -D & 0 \\ 0 & 0 & 0 & 0 \\ 0 & 0 & 0 & 0 \end{vmatrix}. \tag{9}$$

The eigenvalues of A are $\lambda_1 = -\sqrt{me} = -c$, $\lambda_2 = 0$, $\lambda_3 = 0$, and $\lambda_4 = c$. The quantity c represents the speed of light. Since the eigenvalues of A are real, Eq. (8) is hyperbolic.

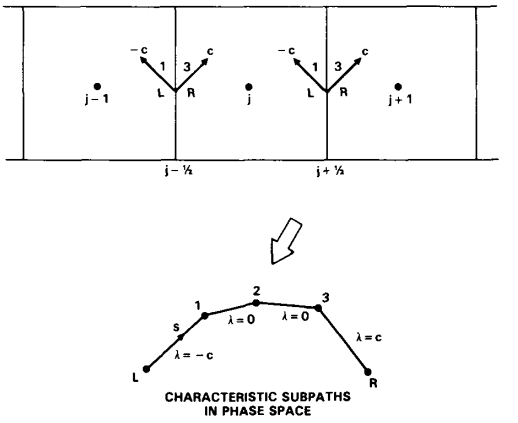

Fig. 4. Numerical flux representation at a cell interface.

Now we construct the numerical flux representation at a cell interface. Referring to Fig. 4 and Eq. (3), the finite-volume treatment requires the evaluation of E at cell faces $j + \frac{1}{2}$ and $j - \frac{1}{2}$, while solving for Q at the cell centroid j. In order to define E at $j + \frac{1}{2}$, we first define a piecewise smooth, continuous path in phase space, connecting Q_j to Q_{j+1}, made up of four subpaths (equaling the number of eigenvalues for the one-dimensional Maxwell equations). Along subpath k, the variation of Q is given by [18]

$$\frac{\partial Q}{\partial s} = r_k(Q(s)) \tag{10}$$

where r_k is the kth eigenvector corresponding to the kth eigenvalue obtained by solving $(A - \lambda_k I)r_k = 0$.

Referring to Fig. 4, Eq. (10) defines the solution vector Q at the end of each characteristic subpath marked by 1, 2, and 3. Starting from the left state $Q_L = Q_j$, across the negative characteristics, the solution vector reaches Q_1, then becomes Q_2 and Q_3 across zero eigenvalue fields, and finally reaches the right state $Q_R = Q_{j+1}$ across the positive characteristics.

Performing the integration of Eq. (10) for each characteristic subpath, the interface electric and magnetic fields are given by

$$\begin{aligned} (Bm)_{j+1/2} &= (B_1 m_1) \\ &= \frac{(c_{j+1}B_{j+1} + D_{j+1}e_{j+1}) + (c_j B_j - D_j e_j)}{(c_j/m_j + c_{j+1}/m_{j+1})} \\ (De)_{j+1/2} &= (D_1 e_1) \\ &= \frac{(c_j D_j - B_j m_j) + (c_{j+1}D_{j+1} + B_{j+1}m_{j+1})}{(c_j/e_j + c_{j+1}/e_{j+1})}. \end{aligned} \tag{11}$$

Use of the characteristic subpath integration approach has resulted in interface flux representation which properly accounts for the variations in material properties ϵ and μ from one cell (j) to the neighboring cell ($j + 1$). Also, the flux form of Eq. (11) guarantees that the flux fields will remain smooth and continuous across the interface, independent of the level of discontinuity in the material property at a cell interface.

V. Transverse Magnetic (TM) and Transverse Electric (TE) Wave Formulation

The Maxwell equations in three dimensions involve three components of the magnetic field (H_x, H_y, and H_z) and three components of the electric field (E_x, E_y, and E_z), which are coupled. In two dimensions, Maxwell's equations can be decoupled into a transverse magnetic (TM) wave and a transverse electric (TE) wave. The TM wave contains only E_z, H_x, and H_y fields, and TE wave contains only H_z, E_x, and E_y fields. For algorithm development, the two-dimensional Maxwell equations in terms of the TM and TE wave framework offer a simplified set of equations without any loss of physics of electromagnetic interaction, including material properties.

The TM and TE equations can be written in a unified form following Eq. (7),

$$Q_t + E_x + F_y = S \tag{12}$$

where Q is a three-element (Q_1, Q_2, Q_3) solution vector, E and F are three-element flux vectors, and S is a source vector containing electric currents.

1) TM wave:

$$\begin{aligned} &Q_1 = D_z \quad E_1 = -Q_3 m \quad F_1 = Q_2 m \quad S_1 = -\sigma Q_1 e \\ &Q_2 = B_x \quad E_2 = 0 \quad\quad F_2 = Q_1 e \quad\; S_2 = 0 \\ &Q_3 = B_y \quad E_3 = -Q_1 e \quad F_3 = 0 \quad\quad S_3 = 0. \end{aligned} \tag{13}$$

2) TE wave:

$$\begin{aligned} &Q_1 = B_z \quad\; E_1 = -Q_3 e \quad F_1 = Q_2 e \quad S_1 = 0 \\ &Q_2 = -D_x \quad E_2 = 0 \quad\quad F_2 = Q_1 m \quad S_2 = -\sigma Q_2 e \\ &Q_3 = -D_y \quad E_3 = -Q_1 m \quad F_3 = 0 \quad\quad S_3 = -\sigma Q_3 e. \end{aligned} \tag{14}$$

Under a body-fitted coordinate transformation, Eqs. (13) take the form [see Eq. (2)]

$$\begin{aligned} &\overline{Q}_1 = \frac{Q_1}{J} \quad\; \overline{E}_1 = -m(Q_2 x_\eta + Q_3 y_\eta) \\ &\overline{Q}_2 = \frac{Q_2}{J} \quad\; \overline{E}_2 = -eQ_1 x_\eta \\ &\overline{Q}_3 = \frac{Q_3}{J} \quad\; \overline{E}_3 = -eQ_1 y_\eta \\ &\overline{F}_1 = m(Q_2 x_\xi + Q_3 y_\xi) \quad \overline{S}_1 = \frac{S_1}{J} \\ &\overline{F}_2 = eQ_1 x_\xi \quad\quad\quad\quad \overline{S}_2 = \frac{S_2}{J} \\ &\overline{F}_3 = eQ_1 y_\xi \quad\quad\quad\quad \overline{S}_3 = \frac{S_3}{J}. \end{aligned} \tag{15}$$

The TE equations [Eqs. (14)] take on similar forms.

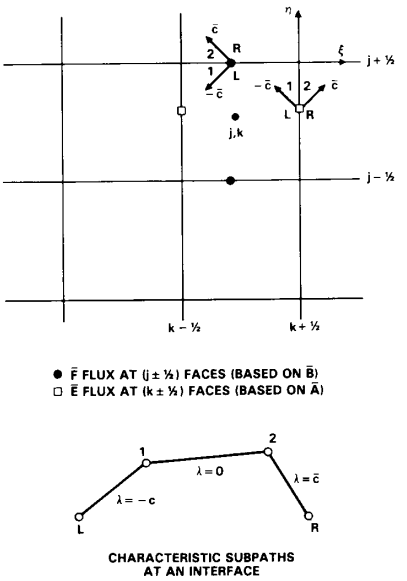

Fig. 5. Characteristics for a two-dimensional finite-volume cell.

It can be verified that the fluxes $\overline{E}_1$ and $\overline{F}_1$ take on the form of surface currents $n \times \mathcal{H}$ or $n \times \mathcal{E}$, depending on whether Eq. (12) is TM or TE.

The characteristics of Eq. (12) are analyzed by considering the Jacobian $\partial\overline{E}/\partial\overline{Q} = \overline{A}$ and $\partial\overline{F}/\partial\overline{Q} = \overline{B}$,

$$\overline{A} = \begin{vmatrix} 0 & m\xi_y & -m\xi_x \\ e\xi_y & 0 & 0 \\ -e\xi_x & 0 & 0 \end{vmatrix}, \quad \overline{B} = \begin{vmatrix} 0 & m\eta_y & -m\eta_x \\ e\eta_y & 0 & 0 \\ -e\eta_x & 0 & 0 \end{vmatrix}. \tag{16}$$

The eigenvalues of $\overline{A}$ and $\overline{B}$ are given by

$$\begin{aligned} &\lambda_{1/A} = -c\sqrt{\xi_x^2 + \xi_y^2} \quad \lambda_{1/B} = -c\sqrt{\eta_x^2 + \eta_y^2} \\ &\lambda_{2/A} = 0 \quad\quad\quad\quad\quad\; \lambda_{2/B} = 0 \\ &\lambda_{3/A} = c\sqrt{\xi_x^2 + \xi_y^2} \quad\; \lambda_{3/B} = c\sqrt{\eta_x^2 + \eta_y^2}. \end{aligned} \tag{17}$$

Any finite-volume-based scheme will require the evaluation of the flux vector $\overline{E}$ (referring to Fig. 5) at the $k + \frac{1}{2}$ cell interface and $\overline{F}$ at the $j + \frac{1}{2}$ interface. Using the characteristic subpath integration procedure [18] in the (ξ, τ) plane at $k + \frac{1}{2}$ and in the (η, τ) plane at $j + \frac{1}{2}$, the following interface relationships are obtained.

At $k + \frac{1}{2}$, the left state material properties correspond to cell k ($e^L = e_k$, $m^L = m_k$) and the right state corresponds to the $k + 1$ cell ($e^R = e_{k+1}$, $m^R = m_{k+1}$). Also, vector $Q^L = Q_k$ and $Q^R = Q_{k+1}$.

$$(eQ_1)_{k+1/2} = \frac{\{(cQ_1)^L - (\overline{Q_2Q_3}m)^L/a_{k+1/2}\} + \{(cQ_1)^R + (\overline{Q_2Q_3}m)^R/a_{k+1/2}\}}{(c/e)^L + (c/e)^R} \tag{18}$$

$$(\overline{Q_2Q_3}m)_{k+1/2} = c^L(Q_1^1 - Q_1^L)a_{k+1/2} + (\overline{Q_2Q_3}m)^L. \tag{19}$$

In Eqs. (18) and (19),

$$a = \sqrt{x_\eta^2 + y_\eta^2}, \qquad \overline{Q_2Q_3} = (Q_2 x_\eta + Q_3 y_\eta).$$

At $j + \frac{1}{2}$,

$$(eQ_1)_{j+1/2} = \frac{\{(cQ_1)^L + (\widehat{Q_2Q_3}m)^L/b_{j+1/2}\} + \{(cQ_1)^R - (\widehat{Q_2Q_3}m)^R/b_{j+1/2}\}}{(c/e)^L + (c/e)^R}$$

$$(\widehat{Q_2Q_3}m)_{j+1/2} = -c^L(Q_1^1 - Q_1^L)b_{j+1/2} + (\widehat{Q_2Q_3}m)^L \tag{20}$$

where $\widehat{Q_2Q_3}m = (Q_2 x_\xi + Q_3 y_\xi)$ and $b = \sqrt{x_\xi^2 + y_\xi^2}$. The superscripts L and R refer to left and right states at $j + \frac{1}{2}$, shown in Fig. 5. The quantities $(\overline{Q_2Q_3}m/a)$ and $(\widehat{Q_2Q_3}m/b)$ represent $n \times \mathcal{H}$ for the TM case and $n \times \mathcal{E}$ for the TE case.

VI. Boundary Conditions

Perfectly Conducting Scattering Surface: For a perfectly conducting scatterer the boundary condition on the surface [20] is

$$n \times \mathcal{E}^T = 0 \tag{21}$$

where $\mathcal{E}^T$ is the total electric field vector and n is the surface outward normal. For the TM case, the boundary condition [Eq. (21)] becomes $\mathcal{E}_z^T = 0$, and for the TE case, $x_\xi \mathcal{E}_x^T + y_\xi \mathcal{E}_y^T = 0$.

Nonperfectly Conducting, Isotropic Scatterer: Let $\mathcal{E}_L^T$, $\mathcal{H}_L^T$ be the total field quantities on the left side of the interface, and $\mathcal{E}_R^T$, $\mathcal{H}_R^T$ on the right side. The boundary conditions at the interface then become (see Fig. 6)

$$n \times (\mathcal{E}_L^T - \mathcal{E}_R^T) = 0, \qquad n \times (\mathcal{H}_L^T - \mathcal{H}_R^T) = 0. \tag{22}$$

The interface flux representations given by Eqs. (18) and (20) strictly satisfy the boundary conditions given by Eq. (22). The boundary conditions at a nonperfectly conducting material interface are also termed "flux through" boundary conditions.

The key advantage of a finite-volume procedure, Eq. (3), employing interface flux representations, Eqs. (18) and (20), arrived at through the use of proper physical theory of characteristic signal propagation, is that no special boundary condition treatment is required to enforce conditions given by Eq. (22). However, at a perfectly conducting surface, the boundary conditions $n \times E = 0$ have to be explicitly satisfied through an appropriate procedure.

Besides the boundary conditions at the scatterer surface, one needs to model the boundary condition at the outer boundary representing the far field in the computational setup. The computational domain terminates at some finite distance from the scatterer, and the domain is usually referred to as "near field." The proper boundary condition at the outer boundary is that the scattered waves smoothly leave the domain without any reflections from the artificial outer boundary. In our work, characteristic theory principles are employed to satisfy the various boundary conditions. The method differs in certain essential respects from that presented by Mur [7] and employed by Taflove and Umashankar [3]–[6]. Details will be given in a follow-up paper.

VII. Lax-Wendroff Explicit Scheme

A finite-volume procedure applied to Eq. (2) is given by Eq. (3). If $n + 1$ is the current time level in which Eq. (3) is satisfied, an implicit scheme would treat all the flux terms at the current level and then employ some form of a flux linearization procedure to solve for Q implicitly [15]–[17]. The main advantage of such implicit techniques in CFD is that they allow for large time steps to be taken in modeling the $\overline{Q}_\tau$ term while maintaining numerical stability. However, the problem of electromagnetic scattering deals with Q and flux fields that are highly oscillatory in both time and space. Implicit schemes that preserve the incident and scattered wave profiles without any numerical distortion for large $\Delta\tau$ are yet to be developed. In view of this, explicit type schemes that operate with stability bounds for $\Delta\tau$ governed by spatial resolution (volume of a finite-volume cell) are more attractive. The disadvantage is that when clustered meshes are used in regions of sharp edges and so on, they may restrict the allowable $\Delta\tau$ to very small values requiring a large number of time steps to establish the solution. Some of the criteria in the selection or construction of an explicit scheme are 1) spatial and temporal accuracy, 2) allowable $\Delta\tau$, usually known as the Courant-Friedrichs-Lewy (CFL) condition [19], [21], [22], 3) storage requirements, and 4) vectorizability of the algorithm.

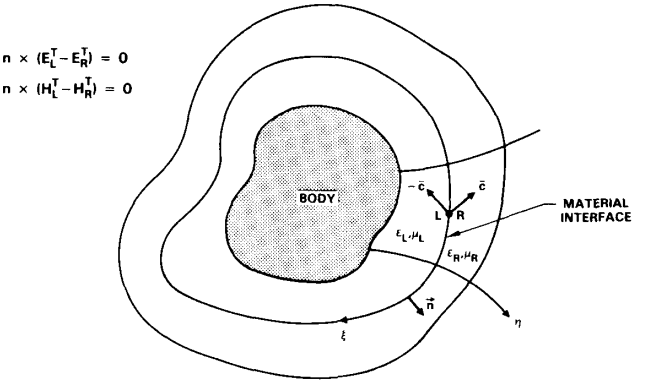

Fig. 6. Boundary conditions at a nonperfectly conducting interface.

One of the explicit schemes widely in use is the Lax-Wendroff upwind scheme [21]. Applied to an equation of the form

$$Q_\tau + F_\eta = 0 \tag{23}$$

the Lax-Wendroff two-step scheme (predictor-corrector) is given by

1) Predictor:

$$\overline{Q^{n+1}} = Q^n - \Delta\tau(\hat{F}^n_{j+1/2} - \hat{F}^n_{j-1/2}). \tag{24}$$

2) Corrector:

$$Q^{n+1} = \frac{1}{2}\{Q^n + \overline{Q^{n+1}} - \Delta\tau(\hat{\overline{F}}^{n+1}_{j+1/2} - \hat{\overline{F}}^{n+1}_{j-1/2})\}$$
$$- \frac{\Delta\tau}{2}[\{(dF)^+_{j-1/2} - (dF)^+_{j-3/2}\}$$
$$- \{(dF)^-_{j+3/2} - (dF)^-_{j+1/2}\}]^n. \tag{25}$$

The predictor step, Eq. (24), is only first-order accurate in time and space. The corrector step makes the scheme second-order accurate in time and space. The addition of the square bracketed term in Eq. (25), evaluated at the nth level, makes the scheme second-order accurate spatially, while the predictor/corrector two-step procedure provides second-order time accuracy.

Referring to Fig. 4,

$$dF^+_{j-1/2} = F^R_{j-1/2} - \hat{F}_{j-1/2}$$
$$dF^-_{j+1/2} = \hat{F}_{j+1/2} - F^L_{j+1/2} \tag{26}$$

where superscripts R and L refer to right and left states at an interface, and $\hat{F}$ refers to flux at an interface. In the present method,

$$F^L_{j-1/2} = F(Q_j, \text{ metrics at } j - \tfrac{1}{2})$$
$$F^R_{j+1/2} = F(Q_{j+1}, \text{ metrics at } j + \tfrac{1}{2}). \tag{27}$$

The Lax-Wendroff scheme being explicit, the allowable $\Delta\tau$ for maintaining numerical stability is bounded by the CFL condition given by

$$\lambda_{\max}\frac{\Delta\tau}{\Delta\eta} \le 2 \tag{28}$$

where $\lambda_{\max}$ is the maximum eigenvalue of the Jacobian, $\partial F/\partial Q$. The condition given by Eq. (28) is for the one-dimensional equation, Eq. (23). In multidimensions, the value of $\lambda_{\max}$ can be taken to be the sum of λ_s in all directions [$\lambda_{\max} = \max(|\lambda_\xi| + |\lambda_\eta| + |\lambda_\zeta|)$]. The maximum eigenvalue usually occurs at a cell that has the least volume.

VIII. Near-Field-to-Far-Field Transformation

The finite-volume procedure of this paper, which solves the time-dependent Maxwell equations, is applied in a computational domain that extends from the scatterer to some finite distance away, where it is terminated by an outer boundary at which nonreflecting boundary conditions are imposed. The distance of the outer boundary of the computational domain is controlled by the body size and the wavelength of the incident wave, and should be sufficiently far away (several wavelengths) where the numerical implementation of the nonreflecting boundary conditions holds. Even when the computational domain extends to several wavelengths from the scatterer, it still represents only the *near-field* solution. However, the bistatic RCS computation is based on the intensity of the scattered wave at distances asymptotically approaching infinity, which means the RCS response represents the *far-field* solution. Using a Green's function based asymptotic approach, the far-field representation of the scattered wave is obtained from the near-field computational solution. A similar approach is also presented in [4].

In general, the RCS response is desired in the frequency domain, whereas the computational solution of this paper is in the time domain. Of course, the advantage of the time-domain approach is that it can accommodate both continuous-wave (single-frequency, harmonic) and single-pulse (multiple-frequency, broad-band) incident fields. Whether the incident wave is a continuous harmonic wave or a single pulse, the time-domain results of electric and magnetic scattered waves are processed using a spectral technique to obtain their response in the frequency domain. Once the near-field response is known in the frequency domain, the bistatic RCS response in the far field is computed. For a continuous wave representing a single frequency, the spectral analysis will provide the response at that given frequency, whereas for a pulse case containing many frequencies, the spectral analysis allows one to compute the RCS response for all frequencies contained in the incident pulse from a single time-domain transient calculation.

IX. Numerical Gridding—Body-Fitted System

As mentioned in Section II, the Cartesian forms of the Maxwell equations are transformed into a body-fitted coordinate system to allow easy implementation of various boundary conditions described in Section VI. Only the independent variables x, y, and z are transformed to ξ, η, and ζ, and the dependent variables [Q vector in Eqs. (1) and (7)] are left in their Cartesian form.

There are two steps involved in setting up a body-fitted coordinate system: 1) definition of the geometry and 2) construction of the field grid points. As shown in Fig. 2, the objective is to set up the grid in the domain bounded by the body surface (1-2-3) on one side and the outer boundary (4-5-6) on the other. A cut in the domain, 1-6 and 3-4, is created to form a four-sided computational domain in two dimensions. In three dimensions, the computational domain will consist of six boundary surfaces. Given the grid point distribution on the computational boundaries (1-2-3 for $\eta_{\min}$, 3-4 for $\xi_{\max}$, 4-5-6 for $\eta_{\max}$, and 6-1 for $\xi_{\min}$), the interior grid can be constructed in many ways [23], both analytical and numerical. The technique followed in this paper is based on an elliptic grid solver approach [24], [25] in which a set of elliptic Poisson equations is solved numerically to generate the grid in physical space,

$$\alpha x_{\xi\xi} - 2\beta x_{\xi\eta} + \gamma x_{\eta\eta} = -J^2(px_\xi + qx_\eta)$$
$$\alpha y_{\xi\xi} - 2\beta y_{\xi\eta} + \gamma y_{\eta\eta} = -J^2(py_\xi + qy_\eta) \tag{29}$$

where $\alpha = x^2_\eta + y^2_\eta$, $\beta = x_\xi x_\eta + y_\xi y_\eta$, and $\gamma = x^2_\xi + y^2_\xi$. The right-hand side $p = p(\xi, \eta)$ and $q = q(\xi, \eta)$ are the forcing terms designed to satisfy desired constraints imposed on the nature of the grid, such as specified grid spacings near boundaries and grid intersection angles. J appearing in Eq. (29) is the Jacobian of the transformation. Details on the

construction of p and q forcing terms are given in [24]. The objective here is to solve Eq. (29) to obtain the (x, y) values of a grid in the physical space corresponding to a given (ξ, η) point in the computational domain.

In a multizone approach, where each structure of the scatterer is gridded separately, the elliptic grid solver given by Eq. (29) will be applied in each zone.

X. Results

Results are presented for both TM and TE two-dimensional cases. In a time-domain formulation, the incident wave can be either continuous (harmonic, single frequency) or a single pulse (Gaussian, square, etc.). Of course, for the computation of a single-pulse transient response, the time-domain solver has to be time accurate, and in the present formulation, the Lax-Wendroff explicit scheme is second-order accurate in both time and space.

For accuracy, the number of grids points on the scatterer to resolve a wavelength of information adequately is taken to be on the order of 8 to 15. This means that, for large bodies (high frequency), the total number of surface grid points to properly resolve the electric and magnetic field distribution can be excessive. However, the present formulation is highly vectorizable and can run efficiently on a supercomputer. If the incident wave is a single pulse containing many frequencies, the number of grid points on the scattering surface must be sufficient to resolve the highest frequency content of the pulse.

A continuous incident wave is represented by (for the TM case)

$$E_z^i = E_0 \cos k(x \cos\theta + y \sin\theta - c_0 t), \qquad k = 2\pi/\lambda_0. \tag{30}$$

The forms for H_x^i and H_y^i are automatically obtained from Maxwell's equation since the incident fields satisfy Maxwell's equations in free space,

$$H_x^i = \frac{E_z^i \sin\theta}{\mu_0 c_0}$$

$$H_y^i = \frac{-E_z^i \cos\theta}{\mu_0 c_0} \tag{31}$$

where θ is the incident angle. Quantities μ_0, $c_0 = 1/\sqrt{\mu_0 c_0}$ represent free-space values usually normalized to 1 ($\epsilon_0 = \mu_0 = c_0 = 1$).

A Gaussian-type incident pulse is represented by

$$E_z^i = E_0 e^{-a^2(x\cos\theta + y\sin\theta - c_0 t)^2} \tag{32}$$

where the parameter a controls the width of the Gaussian.

A. TM Cases

Perfectly Conducting Body in Free Space: For harmonic incident fields, the time-domain calculations are carried out until the scattered fields reach a time harmonic steady state (a few wavelengths of calculation). Then the discrete fast Fourier transforms are employed to obtain the complex field representation in the frequency domain. The bistatic RCS is then computed using a near-field-to-far-field contour integration.

Fig. 7 shows plots of surface currents ($n \times H$) for a square cylinder at two different incident angles, and comparisons

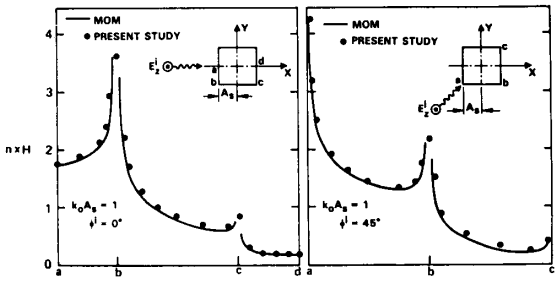

Fig. 7. Surface currents for a perfectly conducting square cylinder.

are made with method of moment (MOM) solutions [4]. Finite-difference time-domain results for this geometry were first presented by Umashankar and Taflove [4]. In contrast to their regular, rectangular mesh, the required grid resolution (at least 10 points per wavelength) is maintained only on and near the body surface. The grid is allowed to stretch along the direction leading away from the surface (nonuniform grid between the body surface and the outer boundary).

Fig. 8 shows bistatic RCS for a circular cylinder and a square cylinder. For accuracy, the contour for RCS evaluation is placed at the centroids of cells neighboring the body surface.

The broad-band frequency response from a single transient calculation using a Gaussian-like incident pulse is demonstrated in Fig. 9. The calculation is started when the

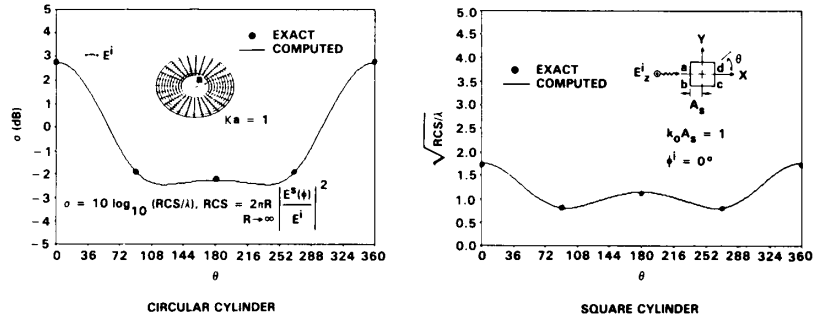

Fig. 8. Two-dimensional RCS calculations.

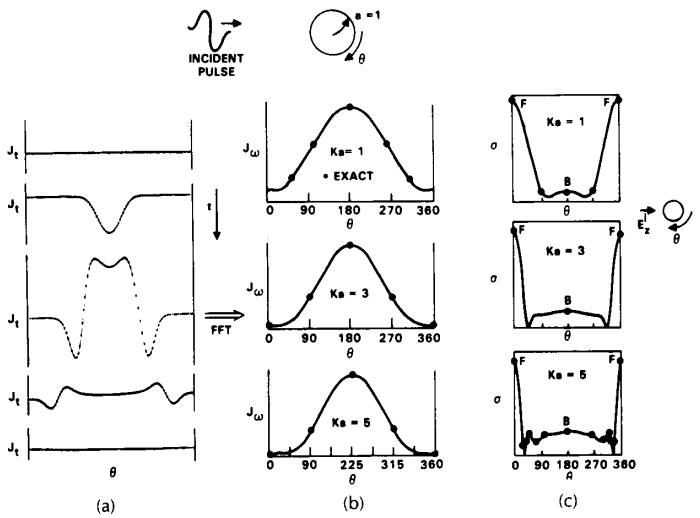

Fig. 9. Transient single-pulse calculations. (a) Surface current in time domain. (b) Surface current in frequency domain. (c) RCS in frequency domain.

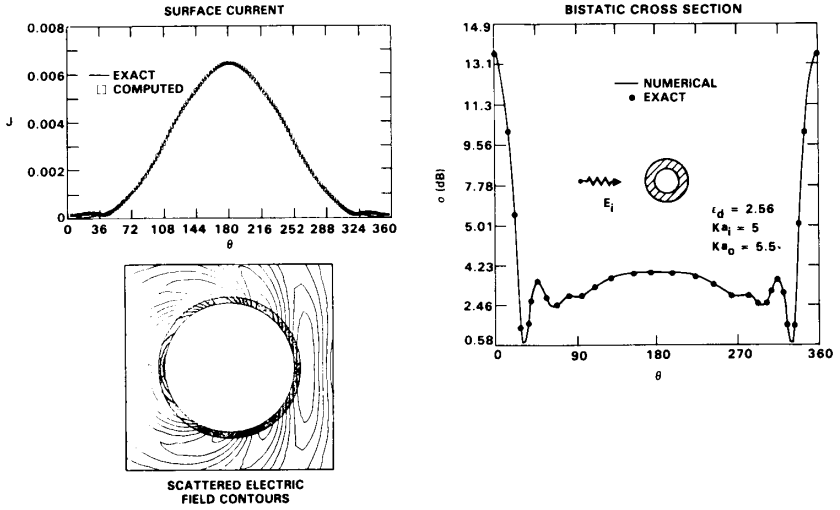

Fig. 10. RCS computation for a conducting cylinder with a dielectric strip.

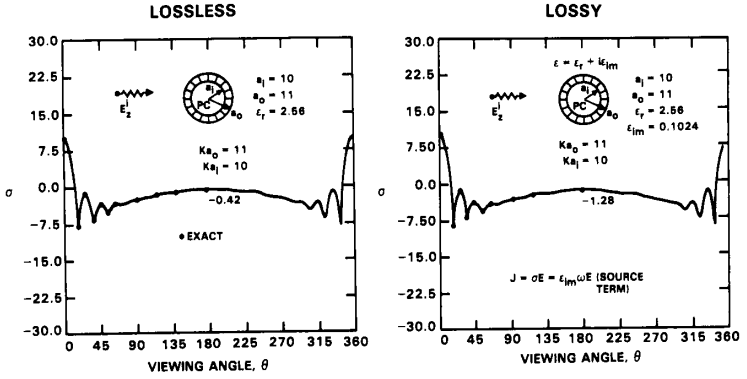

Fig. 11. Effect of lossy coating on RCS.

incident pulse is about to come in contact with the scatterer and is then carried out until the scattered fields completely leave the vicinity of the scattering surface. The transient response is shown in terms of the surface current variation along the body surface in time, which starts as zero at $t = 0$ and gets back to zero at some later time after the transients vanish. This time response is then processed using FFTs to get the field variation in the frequency domain for all frequencies contained in the incident pulse. Then the bistatic RCS as a function of frequency is computed.

Fig. 10 shows results for a perfectly conducting cylinder with a dielectric strip around it. The electric field contours clearly indicate the smoothness of the contours at the interface of free space and dielectric. The characteristic-based Riemann solvers employed at a cell interface ensure such continuity and smoothness of electric and magnetic fluxes. The comparisons of bistatic cross section and surface currents with exact solutions are good.

Fig. 11 shows a similar dielectric strip calculation with and without loss. The lossy material behavior is modeled in terms of an imaginary component to ϵ. The calculation of Fig. 11 for a body size of $Ka = 10$ used 150 grid points along the body and 30 points away from the body. The smallest grid spacing near the body surface is chosen such that nearly 100 time steps will provide a wavelength of calculation.

Fig. 12 shows contours of electric scattered field E_z^s at an instant of time for a circular cylinder. The body at the center

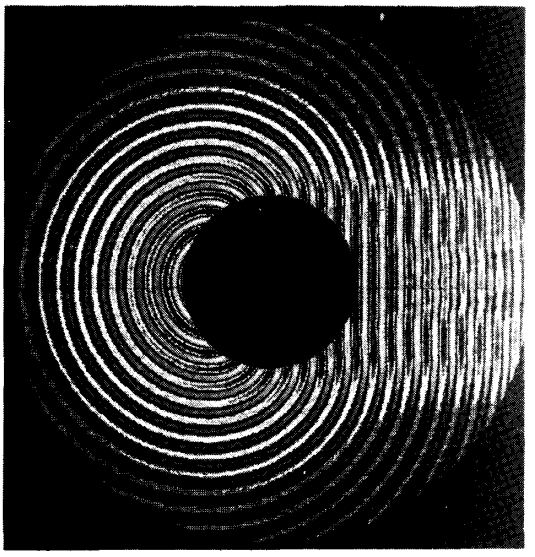

Fig. 12. Scattered electric field contours for a perfectly conducting cylinder.

of the computational domain and the outer boundary are clearly seen. This plot clearly shows that the scattered fields leave the outer boundary smoothly without any noticeable (spurious) reflection. The corresponding total electric field E_z^T contours are shown in Fig. 13. The shadow region is clearly seen.

Fig. 14 shows the bistatic cross section for the NACA 0012 airfoil at different control surface settings. The airfoil is 10 wavelengths long and corresponds to about 1-GHz incident

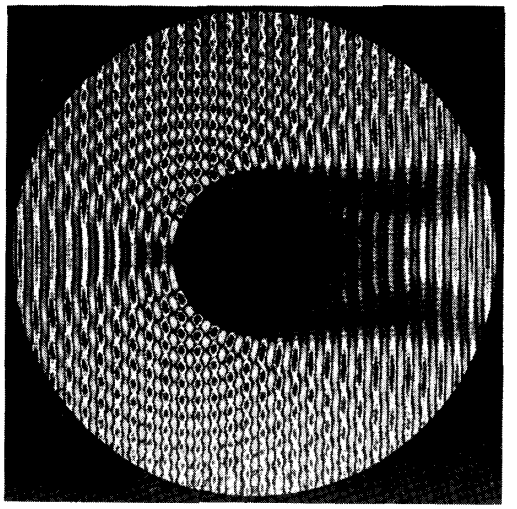

Fig. 13. Total electric field contours for a perfectly conducting cylinder.

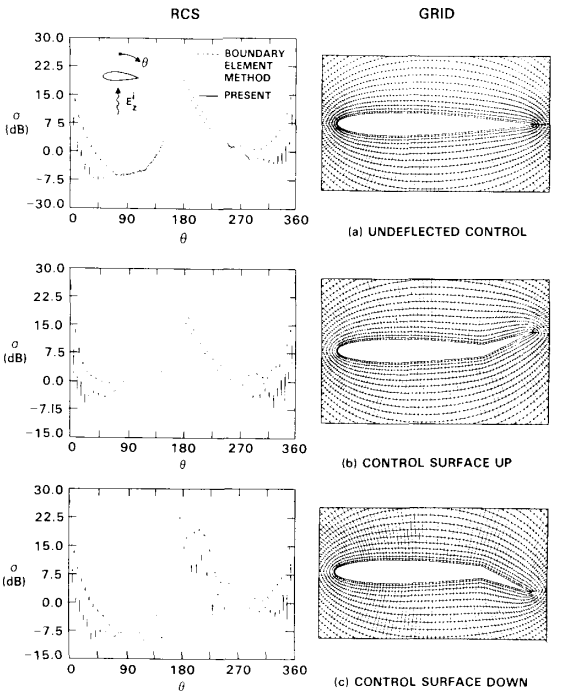

Fig. 14. Scattering from NACA 0012 airfoil.

frequency. The body-fitted gridding for each setting is also shown in the figure.

B. TE Cases

Fig. 15 shows the bistatic RCS for a perfectly conducting cylinder for various Ka values. The variation of σ as a function of viewing angle is more pronounced for the TE cases than for the corresponding TM cases. The computational results compare very well with available exact solutions [20].

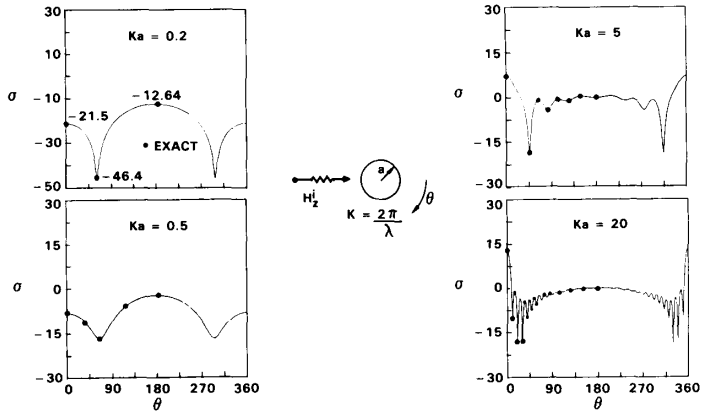

Fig. 15. Two-dimensional TE cases.

Fig. 16 shows bistatic RCS results for a dielectric cylinder ($\epsilon = 2.56$) of $Ka = 1$. This case has a drastic RCS variation in viewing angle. The forward scattering is nearly 0 dB, whereas around the 100° viewing angle the cross section reduces to −60 dB. The finite-volume calculations based on the present formulation seem to produce very accurate results, even for a case having a dynamic range of 60 dB.

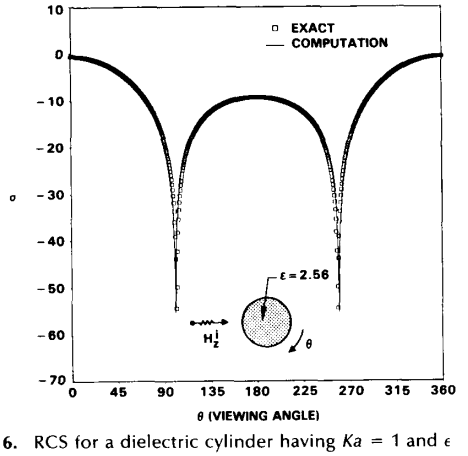

Fig. 16. RCS for a dielectric cylinder having $Ka = 1$ and $\epsilon = 2.56$, TE wave.

Fig. 17 shows the effect of a dielectric shield over a perfectly conducting cylinder. The present method is able to predict the detailed bistatic RCS structure with various nulls quite accurately. Fig. 18 shows a similar case, but with a very large dielectric value of $\epsilon = 100$. This calculation was done using 10 points per wavelength within the dielectric shield. Since the wavelength within the dielectric of $\epsilon = 100$ is 1/10 of the free-space wavelength, the grid spacing with the dielectric material is correspondingly dense, causing the allowable Δt for stable computation [Eq. (28)] to be much smaller than the one used in the computation of Fig. 17. Also, the large material value required many cycles of calculation (nearly 30 cycles) before reaching a time harmonic steady state. Construction of an implicit method having an unconditional stability on Δt is presently under development. Such a method will allow for large Δt values to be used in advancing the solution to a time harmonic steady state.

On a CRAY-X/MP 14 machine, the present two-dimensional code takes 1.2×10^{-6} seconds per time step per grid point. A systematic study of the scaling of computer time has not been carried out, but a rough proportionality to the number of grid points should be observed in both two and three dimensions.

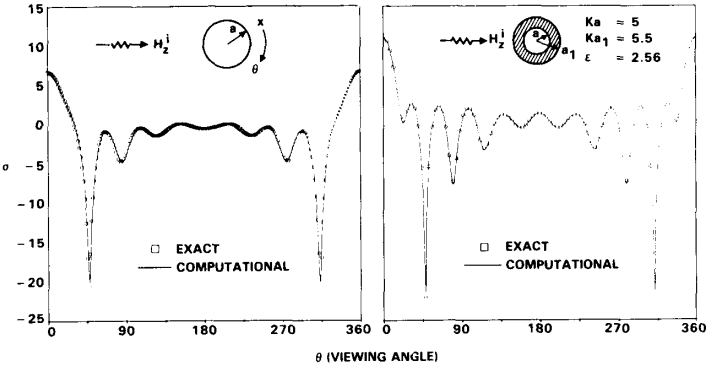

Fig. 17. Bistatic RCS for a perfectly conducting cylinder with (right) and without (left) a dielectric shield.

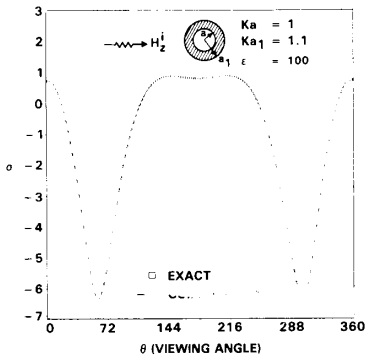

Fig. 18. Application of the time-domain solver for a dielectric shield of large ϵ.

XI. Conclusions

A novel time-domain differential solver for Maxwell's equations utilizing proven numerical algorithms of CFD has been developed and applied to solve the two-dimensional transverse magnetic and transverse electric wave equations. Some of the salient features of this approach are

1) Based on physical theory of characteristic signal propagation as it has been implemented in proven CFD methods
2) Treatment of layered media with discontinuous material properties (lossy and lossless)
3) Numerical gridding for arbitrary geometry treatment
4) Near-field-to-far-field transformation to compute RCS
5) Second-order accurate (time and space) upwind Lax-Wendroff explicit scheme
6) Transient and time harmonic computations
7) Application of fast Fourier transform to derive frequency response from time-domain calculation.

Currently work is under way to extend the two-dimensional solver to full three-dimensional Maxwell equations [26]. Along with the development of a three-dimensional Maxwell equation solver, work is progressing on many fronts. In the algorithm research arena, implicit type schemes are being looked at to avoid CFL (stability) restrictions placed on Δt by the explicit schemes. Modeling of negative material properties ($\epsilon < 0$) which have significance to plasmas and surface polaritons, treatment of thin sheets (resistive cards, lossy coatings, etc.) through appropriate boundary conditions, incorporation of frequency-dependent (time-dependent material properties are easily modeled in a time domain based solver) and nonlinear material properties, gridding requirements for large bodies (high frequency), higher order nonreflecting far-field outer boundary conditions, computer architecture tissues in algorithm design (coarse-grain and fine-grain parallel processing), etc., are some of the topics of interest.

Acknowledgment

The authors would like to express their sincere appreciation to Dr. Sukumar Chakravarthy and Professor Stanley Osher for many valuable discussions and to Mr. Barna Bihari and Miss Kimberly Peppi for their support of computer graphics.

References

[1] K. S. Yee, "Numerical solution of initial boundary value problems involving Maxwell's equations in isotropic media," *IEEE Trans. Antennas Propagat.*, vol. AP-14, pp. 302–307, 1966.
[2] E. K. Miller, A. J. Poggio, and G. J. Burke, "An integro-differential equation technique for time-domain analysis of thin-wire structures; Part I—The numerical method," *J. Comput. Phys.*, vol. 12, p. 24, 1973.
[3] A. Taflove and K. Umashankar, "A hybrid moment method/finite-difference time domain approach to electromagnetic coupling and aperture penetration into complex geometries," *IEEE Trans. Antennas Propagat.*, vol. AP-30, pp. 617–627, 1982.
[4] K. Umashankar and A. Taflove, "A novel method to analyze electromagnetic scattering of complex objects," *IEEE Trans. Electromag. Compat.*, vol. EMC-24, pp. 397–405, Nov. 1982.
[5] A. Taflove and K. R. Umashankar, "Radar cross section of general three-dimensional scatterers," *IEEE Trans. Electromag. Compat.*, vol. EMC-25, pp. 433–440, Nov. 1983.
[6] ——, "The finite-difference time-domain (FD-TD) method for electromagnetic scattering and interaction problems," *J. Electromag. Waves Appl.*, vol. 1, no. 3, pp. 243–267, 1987.
[7] G. Mur, "Absorbing boundary conditions for the finite-difference approximation of the time-domain electromagnetic field equations," *IEEE Trans. Electromag. Compat.*, vol. EMC-23, pp. 377–382, Nov. 1981.
[8] A. C. Cangellaris, C. C. Lin, and K. K. Mei, "Point-matched time domain finite element methods for electromagnetic radiation and scattering," *IEEE Trans. Antennas Propagat.*, vol. AP-35, pp. 1160–1173, Oct. 1987.
[9] V. Shankar, S. Chakravarthy, and K.-Y. Szema, "Development and application of CFD methods to problems in computational science," Workshop on CFD for Aerospace Problems, Univ. of Tennessee Space Institute, UTSI Publ. E02-4005-013-88, Mar. 7–11, 1988.
[10] V. Shankar, K.-Y. Szema, and S. Osher, "A conservative type-dependent full potential method for the treatment of supersonic flows with embedded subsonic regions," *AIAA J.*, vol. 23, no. 1, pp. 41–48, 1985.
[11] V. Shankar, H. Ide, J. Gorski, and S. Osher, "A fast, time-accurate unsteady full potential scheme," *AIAA J.*, vol. 25, Feb. 1987.
[12] V. Shankar and H. Ide, "Unsteady full potential computations for complex configurations," presented at the AIAA 25th Aerospace Sciences Mtg., Reno, NV, Jan. 1987.
[13] S. R. Chakravarthy, D. A. Anderson, and M. D. Salas, "The split-coefficient matrix method for hyperbolic systems of gas-dynamic equations," presented at the AIAA 18th Aerospace Sciences Mtg., Pasadena, CA, Jan. 14–16, 1980.
[14] S. R. Chakravarthy and K.-Y. Szema, "An Euler solver for three-dimensional supersonic flows with subsonic pockets," presented at the AIAA 18th Fluid Dynamics, Plasmadynamics, and Lasers Conf., Cincinnati, OH, July 16–18, 1985.
[15] K.-Y. Szema, S. R. Chakravarthy, and H. Dresser, "Multizone Euler marching technique for flows over multibody configurations," AIAA papers 87-0592, Jan. 1987, and 88-0276, Jan. 1988.
[16] S. R. Chakravarthy and D. K. Ota, "Numerical issues in computing inviscid supersonic flow over conical delta wings," presented at the AIAA 24th Aerospace Sciences Mtg., Reno, NV, Jan. 6–9, 1986.
[17] P. L. Roe, "Approximate Riemann solvers, parameter vectors, and difference schemes," *J. Comput. Phys.*, vol. 43, pp. 357–372, 1981.
[18] S. Osher and S. R. Chakravarthy, "High resolution schemes and the entropy conditions," *SIAM J. Numer. Anal.*, vol. 21, pp. 955–984, Oct. 1984.
[19] P. Lax, "Hyperbolic systems of conservation laws and the mathematical theory of shock waves," SIAM, Philadelphia, PA, 1973.
[20] G. T. Ruck, D. E. Barrick, W. D. Stuart, and C. K. Krichbaum, *Radar Cross Section Handbook*, vols. 1 and 2. New York, NY: Plenum, 1970.

[21] R. F. Warming and R. M. Beam, "Upwind second-order difference schemes and applications in aerodynamic flows," *AIAA J.*, vol. 14, Sept. 1976.
[22] R. Courant, K. Friedrichs, and H. Lewy, "On the partial difference equations of mathematical physics," *IBM J.*, pp. 215–234, Mar. 1967.
[23] J. F. Thompson, F. C. Thames, and C. W. Mastin, "Automatic numerical generation of body-fitted curvilinear coordinate system for field containing any number of arbitrary two-dimensional bodies," *J. Comput. Phys.*, vol. 15, pp. 299–319, July 1974.
[24] J. L. Steger and R. L. Sorenson, "Automatic mesh-point clustering near a boundary in grid generation with elliptic partial differential equations," *J. Comput. Phys.*, vol. 33, pp. 405–410, Dec. 1979.
[25] V. Shankar and S. Rudy, "Application of a two-dimensional grid solver for three-dimensional problems," *AIAA J.*, vol. 23, Mar. 1985.
[26] V. Shankar, W. F. Hall, and A. Mohammadian, "A three-dimensional Maxwell's equation solver for computation of scattering from layered media," presented at the 3rd Biennial IEEE Conf. on Electromagnetic Field Computation, Bethesda, MD, Dec. 12–14, 1988.

Vijaya Shankar received the M.S. and Ph.D. degrees in aerospace engineering from Iowa State University of Science and Technology, Ames, in 1977.

He is Director, Computational Sciences Function, of the Rockwell International Science Center, Thousand Oaks, CA, where he conducts and coordinates research in linear and nonlinear mechanics, involving a wide variety of problems in mathematical physics such as computational fluid dynamics and electromagnetic scattering. He has 40 publications in the technical literature.

Dr. Shankar is a Fellow of the American Institute of Aeronautics and Astronautics (AIAA). He was the recipient of the 1975 National Student Award and the 1985 Lawrence Sperry Award from AIAA, the 1985 Rockwell Engineer of the Year award, the 1985 Outstanding Young Alumnus Award from Iowa State University, and the 1986 NASA Medal for Public Service. He is Chairman of Rockwell's Fluid Dynamics Technical Panel and Associate Editor of the *AIAA Journal*.

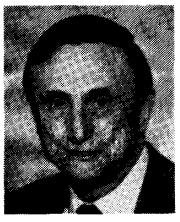

William. F. Hall received the Ph.D. degree in physics from the University of California in 1964.

From 1961 to 1964 his work experience entailed preliminary design for guidance, navigation, and control systems at Northrop Nortronics, Palos Verdes, CA. From 1965 to the present, he has worked as a Research Physicist, Member of Technical Staff, and currently Group Leader at the Rockwell Science Center. In 1970 he was Coinstructor, Mathematical Methods in Research, at Harvey Mudd College, Claremont, CA, funded under a Sloan Foundation grant to explore new methods in teaching. He has made significant scientific contributions in the following areas. 1) Charged-particle scattering in crystals: His work with R. E. DeWames and G. W. Lehman was the first to point out and evaluate the importance of quantum effects in channeling, a phenomenon in which charged particles penetrate a crystal lattice to great depths. In later work, the conditions which govern the transition of this phenomenon from quantum to classical behavior were established. 2) Properties of magnetic systems: He has contributed to the understanding of a wide range of phenomena in magnetic systems, including magnetic bubble-domain dynamics, surface magnetization near the transition temperature, and thermal properties of the magnetization in the vicinity of a magnetic impurity. 3) Viscoelastic effects in polymer solutions: With R. E. DeWames and M. C. Shen, he has investigated and extended the currently accepted theories of the frequency-dependent viscosity in polymer solutions, applying these theories to the calculation of the relaxation-time spectrum of block copolymers. 4) Characteristics of compound semiconductor interfaces: He has derived a relationship between the current–voltage characteristic of a semiconductor heterojunction and the variation in material properties in the vicinity of metallurgical interface. In conjunction with W. E. Tennant, J. Cape, and J. S. Harris, he has developed an optical technique for probing the position dependence of the bandgap near the interface. In addition to his research in the above areas, he has collaborated in the investigation of a number of diverse topics, including distributed-feedback lasers, magnetic suspension viscosity, dielectric properties of salt solutions, and various applications of electromagnetic theory.

Dr. Hall is a member of the American Physical Society, Pi Mu Epsilon, and Sigma Pi Sigma, and has 40 publications.

Alireza H. Mohammadian (Member, IEEE) received the engineering degree from the University of Tehran in 1971, the M.S. degree from Michigan Technological University, Houghton, in 1976, and the Ph.D. degree from the University of Michigan, Ann Arbor, in 1980, all in electrical engineering.

He worked at Iran Telecommunication Research Center (ITRC) from 1971 to 1975, of which he spent six months at Nippon Telegraph & Telephone Public Corporation in Japan. There he conducted research on microwave propagation in desert areas and also statistical analysis of radio refractivity near the ground. In 1980 he joined the Iranian Telecommunication Manufacturing Company (ITMC) as Director of Engineering. From December 1982 to August 1983, he was a Postdoctoral Research Associate in the Department of Electrical and Electronic Engineering at the University of Adelaide, Australia, where he was engaged in research on the mutual coupling effect in microstrip antenna arrays. Later he joined ANTECH Antenna Technologies in Kirkland, Canada, where he worked on microwave antennas. In 1984 he became Assistant Professor of Electrical and Computer Engineering at the University of Michigan, Dearborn. He is at present with the Rockwell International Science Center, Thousand Oaks, CA. His research interests include electromagnetic transients, dyadic Green's functions, printed antennas, antenna arrays, and electromagnetic interference and compatibility.

Dr. Mohammadian is a member of Tau Beta Pi and Sigma Xi.